Electronic Supplementary Information

Nitrate-coordinated FeNi(OH)$_2$ for hydrazine oxidation assisted seawater splitting at the industrial-level current density

Baghendra Singh,[a] Rakesh Kumar,[a] Toufik Ansari,[b] Arindam Indra,[b,]* and Apparao Draksharapu[a,]*

[a]Southern Laboratories - 208A, Department of Chemistry, Indian Institute of Technology Kanpur, Kanpur-208016 (India).

E-mail: appud@iitk.ac.in

[b]Department of Chemistry, Indian Institute of Technology BHU, Varanasi-221005 (India).

E-mail: arindam.chy@iitbhu.ac.in

Chemicals

All chemicals utilized in the synthesis of catalysts were analytical grade and used in synthetic process without any further purification. Nickel foam was purchased from Kanopy Techno Solutions Pvt. Ltd. Pune, India. Double distilled water was used for the synthesis and electrochemical measurements. Nickel(II) nitrate hexahydrates ($[Ni(NO_3)_2].6H_2O$), and iron(III) nitrate nonahydrate ($[Fe(NO_3)_3].9H_2O$) were obtained from S.D. Fine chemicals limited.

Experimental Section

1. Activation of nickel foam[1]

1 cm x 2 cm size NF pieces were washed with acetone followed by multiple time washings with double distilled water. The clean NF pieces were sonicated in 1.0 M HCl for 10 minutes, followed by washings with double distilled water and dried at 50 °C in an air oven for 12 h.

2. Synthesis of nitrate coordinated nickel hydroxide [N_C-Ni(OH)$_2$]

A 50 ml flask containing 10 g of $Ni(NO_3)_2 \cdot 6H_2O$ was placed in an oven at 125 °C for 20 minutes until the salt was completely melted. Subsequently, the cleaned NF was dipped into the molten salt and reacted at 125 °C for 10 hours. The resulting N_C-Ni(OH)$_2$ was then washed with deionized water and ethanol.

3. Synthesis of nitrate coordinated iron-nickel hydroxide [N_C-FeNi(OH)$_2$]

The synthesized N_C-Ni(OH)$_2$ was immersed in 6 mL 1.5 M $Fe(NO_3)_3 \cdot 6H_2O$ solution at 80 °C for 2 h to synthesize N_C-FeNi(OH)$_2$. For the comparison purpose, N_C-FeNi(OH)$_2$-1 and N_C-FeNi(OH)$_2$-2 were also prepared by immersing N_C-Ni(OH)$_2$ in 1.0 M $Fe(NO_3)_3 \cdot 6H_2O$ and 2.0 M $Fe(NO_3)_3 \cdot 6H_2O$, respectively.

4. Synthesis of nitrate intercalated iron-nickel hydroxide [N_I-FeNi(OH)$_2$]

The N_I-FeNi(OH)$_2$ was synthesized by hydrothermal method. A mixture was prepared by dissolving 1 mmol $Ni(NO_3)_2 \cdot 6H_2O$, 1 mmol $Fe(NO_3)_3 \cdot 9H_2O$, 4 mmol NH_4F and 10 mmol NH_2CONH_2 in water (12 mL). The mixture was placed into a 40 mL Teflon coated autoclave and pieces of NF were immersed vertically inside the mixture. The autoclave was sealed and

heated at 120 $^{\circ}$C for 5 h. After normal cooling to room temperature, the synthesized films of N_I-FeNi(OH)$_2$ were washed with water and ethanol and then dried in an air oven at 50 $^{\circ}$C for 12 h.

Characterization

The crystal structure and phases of synthesized catalysts were determined by using power X-ray diffraction (PXRD). The PXRD measurement was done by the PANalytical Xpert powder diffractometer with an incident radiation of Cu-Kα (0.154 nm) in the 2θ range of 5° to 80° with a step size of 0.01°.

The valence states of the elements in the synthesized catalysts were evaluated by X-ray photoelectron spectroscopy (XPS) using PHI 5000 Versa Prob II model. The sample was prepared like PXRD but on a very thin glass slide. The software used for XPS data fitting was Origin Pro 8.5. The morphological characteristics were examined using scanning electron microscopy (SEM) with JEOL JSM-6010LA Tungsten-Electron Microscope(W-SEM); and dispersive X-ray (EDX) analysis was carried out using integrated EDS. The study of transmission electron microscopy (TEM) was performed using Tecnai G2 20 TWIN transmission electron microscope.

Electrochemical measurements

The measurement of electrochemical performance of synthesized catalyst was carried out in a single three-electrode electrochemical cell in 1.0 M aqueous KOH solution and real alkaline seawater. The catalysts synthesized on nickel foam were utilized as working electrode and Pt wire was used in form of counter electrode. The Ag/AgCl was used as reference electrode. All the electrochemical experiments were performed in 1.0 M KOH solution and real alkaline seawater with or without 0.1 M hydrazine.

Cyclic voltammetry (CV) and linear sweep voltammetry (LSV) were performed and expressed with 70% iR correction. All the potential measurements were converted into reversible hydrogen electrode (RHE) by using the formula:

$$E(RHE) = E(Ag/AgCl) + 0.197 + 0.059 \, pH$$

The frequency range in electrochemical impedance spectroscopy (EIS) was from 0.001 to 100,000 Hz and amplitude of 10 mV. The calculations of charge transfers resistance (Rct) were performed from the diameter of the semicircle in the Nyquist plots. The experiment of chronoamperometric measurement (CA) was carried out in 1.0 M KOH solution at a particular constant potential and presented without iR compensation. The Tafel slope was determined at the potentials where current density was reached up to 10 mA cm^{-2}. The cyclic voltammetry (CV) for the C_{dl} measurement was performed at a potential range where apparent faradaic process did not occur.

Detection of ClO⁻ formation

The anodic oxidation of Cl⁻ leads to the formation of Cl$_2$, which subsequently reacts with hydroxide ions to produce ClO⁻ through the following reaction.

$$Cl_2 + 2OH^- \leftrightarrow Cl^- + ClO^- + H_2O$$

The o-tolidine test was conducted to detect the presence of ClO⁻ in the electrolyte solution. To prepare the o-tolidine indicator solution, 10 mg of o-tolidine was dissolved in 1.5 mL of concentrated hydrochloric acid and then diluted to 10 mL. After the CA tests, 400 μL of the electrolyte solution was extracted for ClO⁻ detection. This sample was combined with 400 μL of 0.5 M H$_2$SO$_4$, followed by the addition of 1200 μL of the o-tolidine solution. The reaction of ClO⁻ with *o*-tolidine can be expressed as:

o-tolidine   *o*-tolidine-ox (λ_{max} = 437 nm)
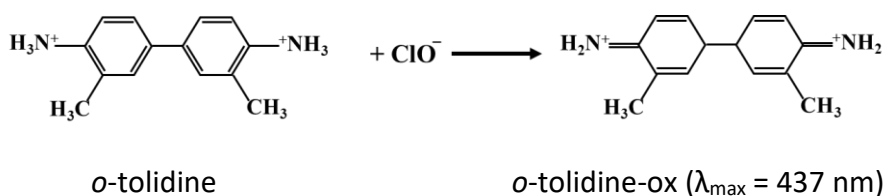
If ClO⁻ was formed, the solution would change color from colorless to yellow. Additionally, the UV-vis spectrum was used to detect *o*-tolidine-ox. The UV-Vis spectra did not show any absorption band at 437 nm (Figure S25).
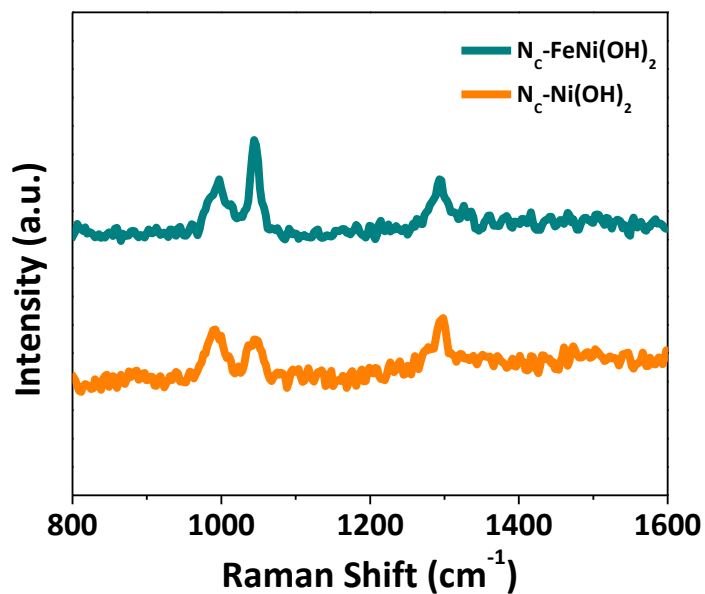
Figures

Figure S1. Raman spectra of N_C-FeNi(OH)$_2$ and N_C-Ni(OH)$_2$. The peaks at 1295, 1044 and 995 cm^{-1} were attributed to NO$_3^-$. The peaks at 1295 and 995 cm^{-1} indicate the antisymmetric stretching vibrations of O-N-O. The signal at 1044 cm^{-1} is corresponding to the symmetric stretching vibration of O-N-O. These characteristic peaks indicate that NO$_3^-$ is monodentate and an oxygen atom of NO$_3^-$ is coordinated with metal Ni.[2]
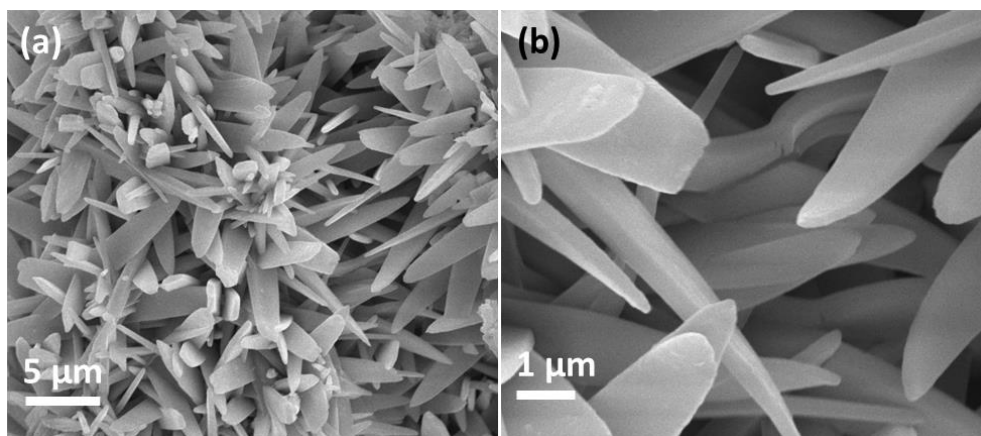

Figure S2. (a-b) SEM images of N_C-Ni(OH)$_2$ showing the nanowire morphology.
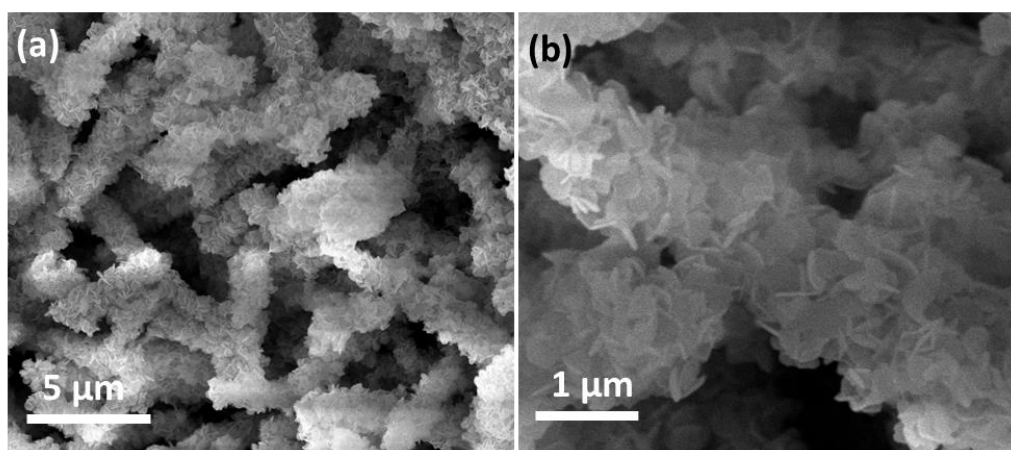
Figure S3. (a-b) SEM images of N_C-FeNi(OH)$_2$ showing the nanosheet morphology.
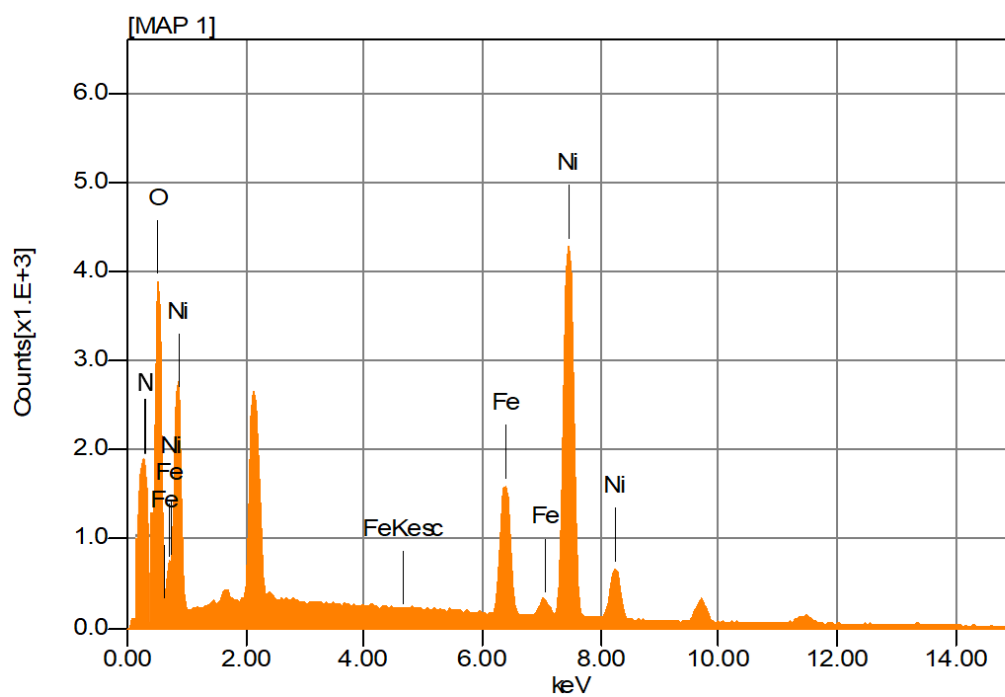
Figure S4. EDX spectrum of N_C-FeNi(OH)$_2$ showing the presence of Ni, Fe, N and O elements.
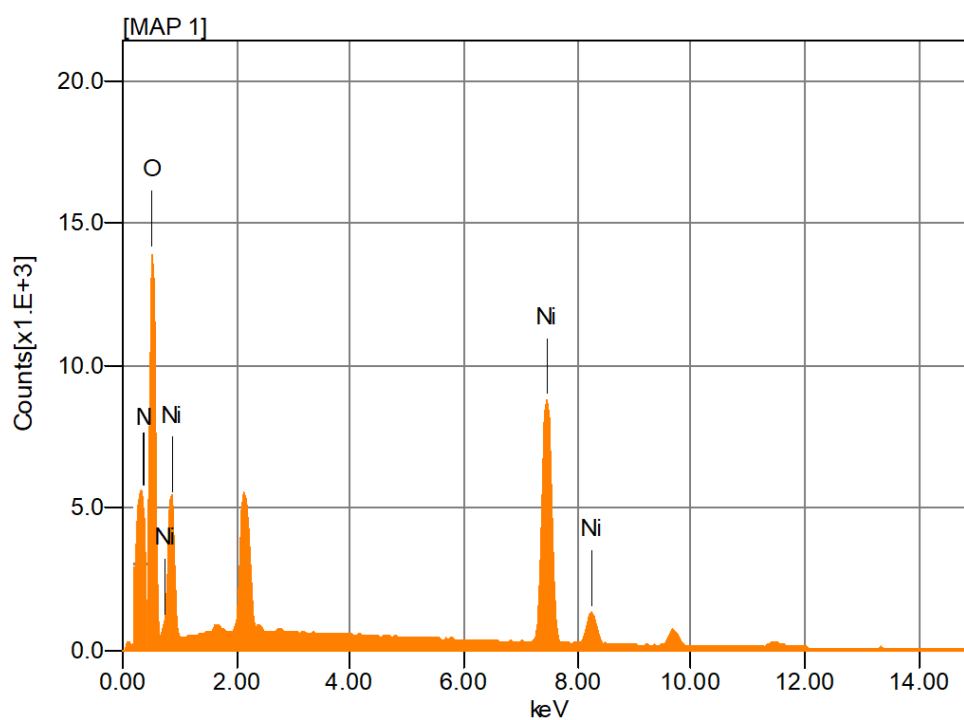
Figure S5. EDX spectrum of N_C-Ni(OH)$_2$ indicating the presence of Ni, N and O elements.

Table S1. Composition of the catalyst measured from EDX and XPS.

Catalyst	Ni (%) (EDX)	Ni (%) (XPS)	Fe (%) (EDX)	Fe (%) (XPS)	N (%) (EDX)	N (%) (XPS)	O (%) (EDX)	O (%) (XPS)
N_C-FeNi(OH)$_2$	34.31	35.54	7.30	8.12	6.75	7.21	51.64	49.13
N_C-Ni(OH)$_2$	29.47	31.12	-	-	7.23	7.98	63.13	60.9
N_C-FeNi(OH)$_2$-CA	43.49	44.76	3.23	3.89	4.86	8.89	48.42	42.46
N_C-Ni(OH)$_2$-CA	33.43	34.65	-	-	5.21	9.12	61.36	56.23
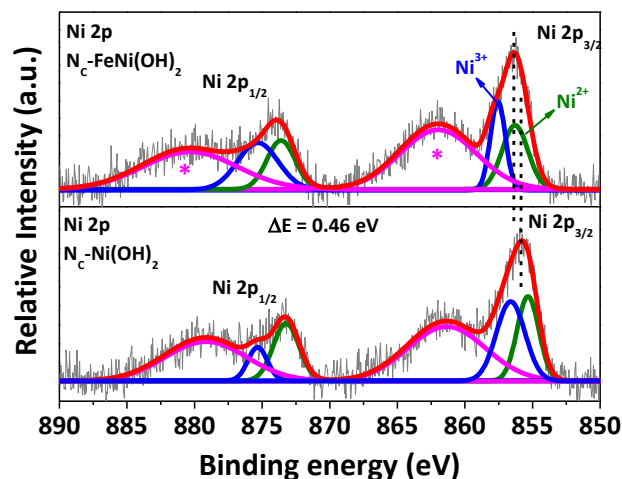
Figure S6. Comparison of Ni 2p XPS of N_C-FeNi(OH)$_2$ and N_C-Ni(OH)$_2$. The peaks at 856.38 eV and 873.96 eV in N_C-FeNi(OH)$_2$ correspond to Ni 2p$_{3/2}$ and Ni 2p$_{1/2}$, respectively.[1,2] The Ni^{2+} and Ni^{3+} peaks were observed at 855.79 eV and 857.30 eV. The Ni 2p$_{3/2}$ XPS peak in N_C-FeNi(OH)$_2$ showed a shift of 0.46 eV towards higher binding energy compared to N_C-Ni(OH)$_2$. Furthermore, the peak area intensity ratio of Ni^{3+}/Ni^{2+} in N_C-FeNi(OH)$_2$ was significantly higher at 1.48, compared to 1.23 in N_C-Ni(OH)$_2$. * marked peaks were ascribed to the satellite peak.[1]
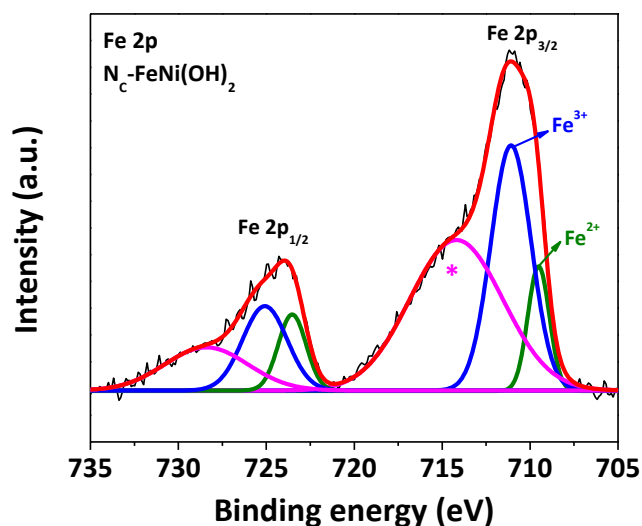
Figure S7. Fe 2p XPS of N_C-FeNi(OH)$_2$. The peaks at 711.11 eV and 723.97 eV originated for Fe 2p$_{3/2}$ and Fe 2p$_{1/2}$, respectively.[3,4] The Fe 2p$_{3/2}$ peak was further fitted into two peaks at 709.53 eV and 711.04 eV for the Fe^{2+} and Fe^{3+} species, respectively. * marked peak was ascribed to the satellite peak.[3,4]
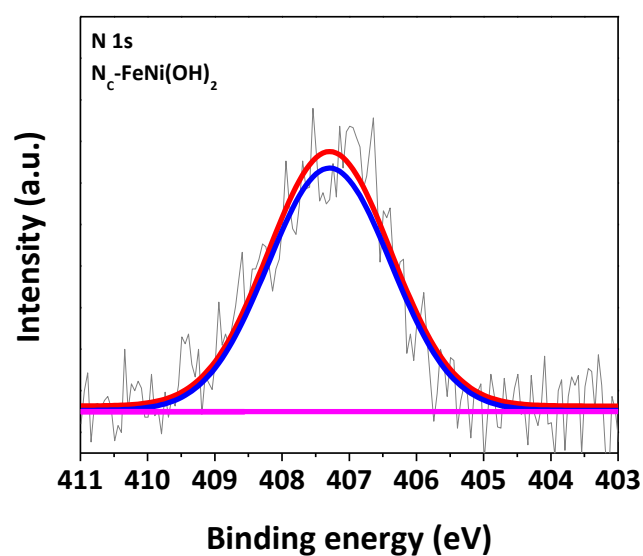
Figure S8. N 1s XPS of N_C-FeNi(OH)$_2$ showing the peak at 407.32 eV corresponding to the metal-nitrate bond.[2]
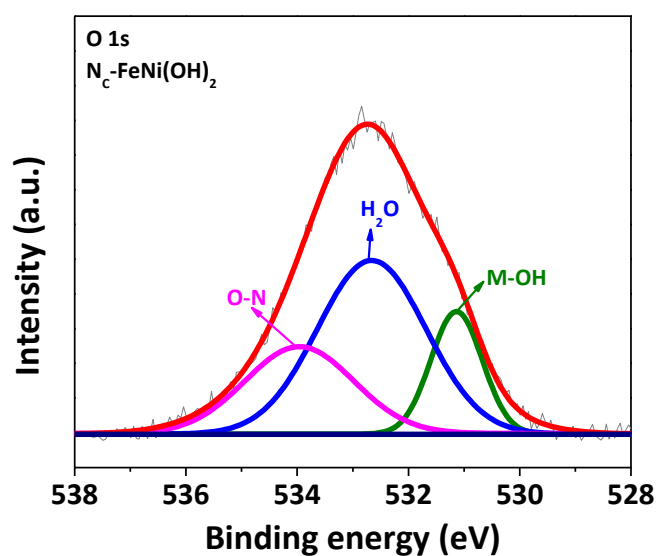

Figure S9. O 1s XPS of N_C-FeNi(OH)$_2$. The peaks were originated from M-OH group (531.14 eV), adsorbed water on the surface (532.68 eV) and O−N bond from NO_3^- (533.96 eV).[3,4]
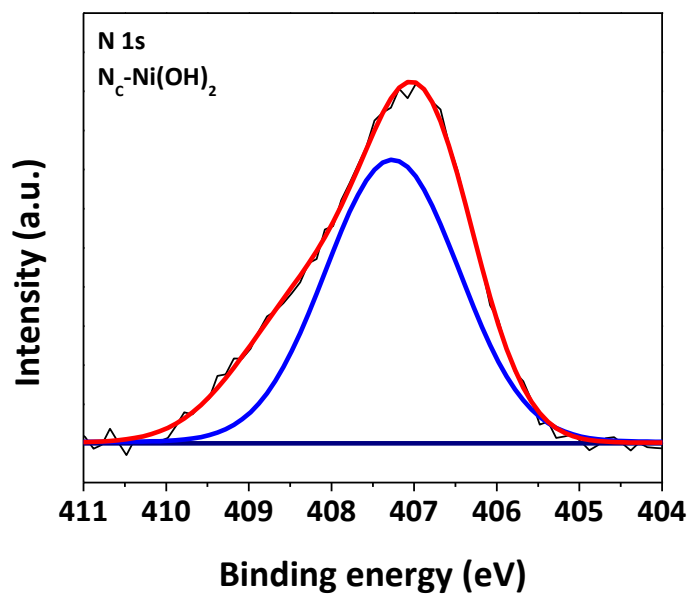
Figure S10. N 1s XPS of N_C-Ni(OH)$_2$ showing the peak at 407.21 eV corresponding to the metal-nitrate bond.[2]
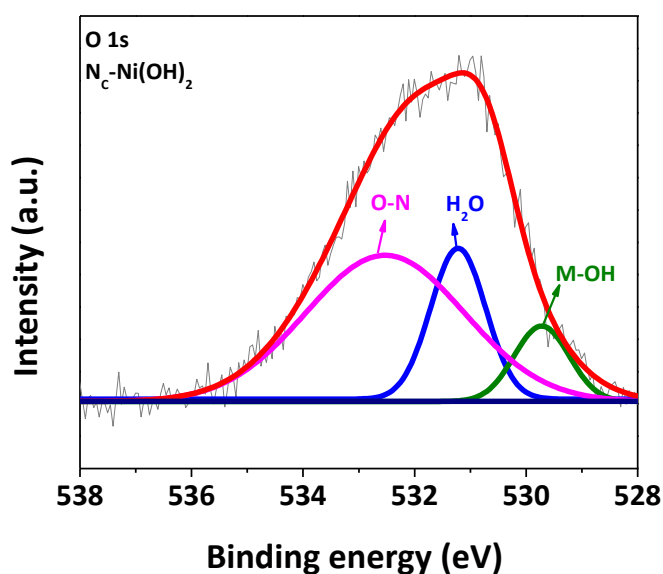

Figure S11. O 1s XPS of N_C-Ni(OH)$_2$. The peaks were originated from M-OH group (529.73 eV), adsorbed water on the surface (531.21 eV) and O–N bond from NO_3^- (532.55 eV).[3,4]
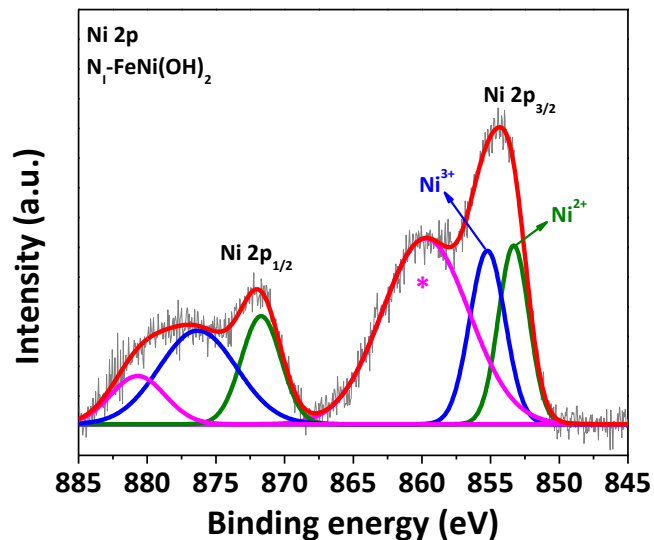
Figure S12. Ni 2p XPS of N_I-FeNi(OH)$_2$. The peaks at 854.38 eV and 872.04 eV in N_I-FeNi(OH)$_2$ correspond to Ni 2p$_{3/2}$ and Ni 2p$_{1/2}$, respectively.[5,6] The Ni^{2+} and Ni^{3+} peaks were observed at 853.29 eV and 855.25 eV. The Ni 2p$_{3/2}$ XPS peak in N_I-FeNi(OH)$_2$ showed a shift of 2.00 eV towards lower binding energy compared to N_C-FeNi(OH)$_2$. * marked peak was ascribed to the satellite peak.
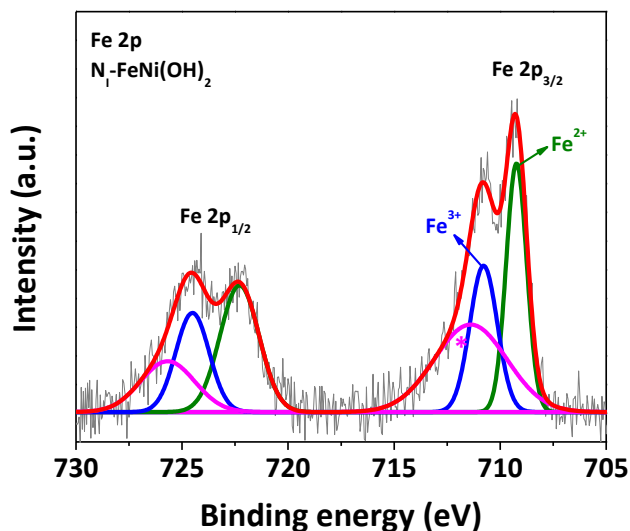

Figure S13. Fe 2p XPS of N_I-FeNi(OH)$_2$. The peaks at 709.27 eV and 722.30 eV originated for Fe 2p$_{3/2}$ and Fe 2p$_{1/2}$, respectively. The Fe 2p$_{3/2}$ peak was further fitted into two peaks at 709.23 eV and 710.81 eV for the Fe^{2+} and Fe^{3+} species, respectively. * marked peak was ascribed to the satellite peak.[3,4]
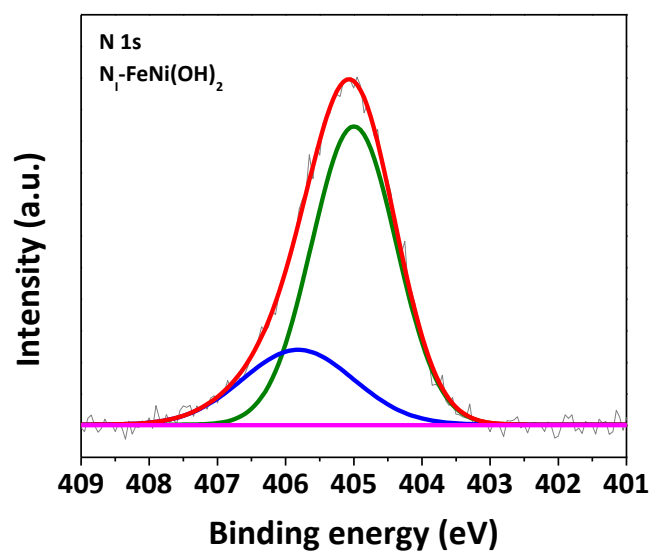
Figure S14. N 1s XPS of N$_I$-FeNi(OH)$_2$ showing the peaks at 404.98 eV and 405.82 eV corresponding to NO$_3^-$ and N-O bond.[2]
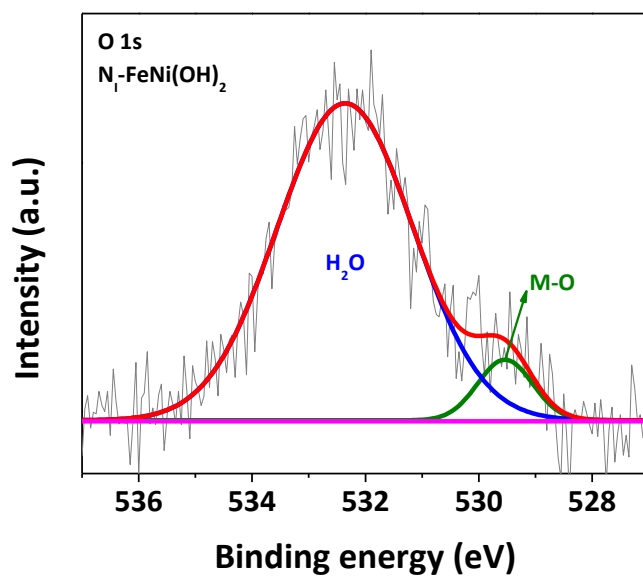

Figure S15. O 1s XPS of N$_I$-FeNi(OH)$_2$. The peaks showed two peaks at 529.52 eV and 532.38 eV, attributed to the M-O bond and adsorbed H$_2$O molecules, respectively.[3,4]
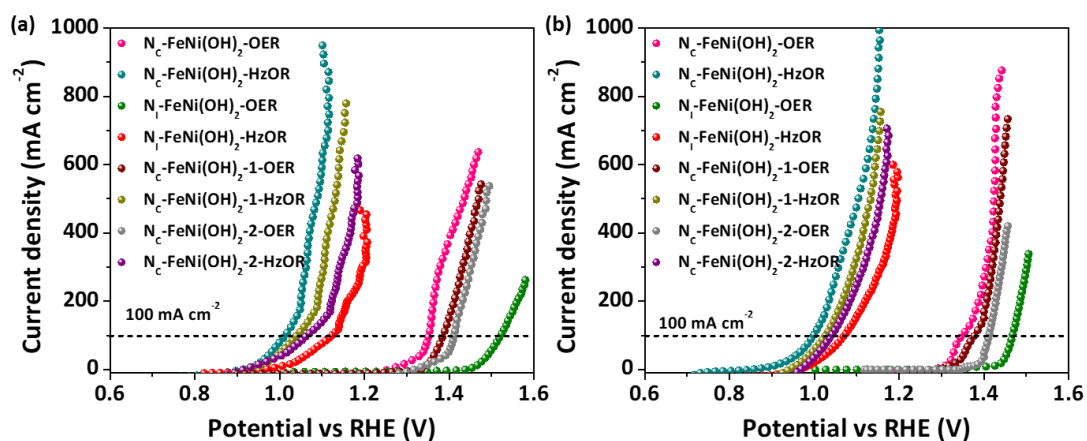
Figure S16. (a) LSV profiles for the seawater OER and hydrazine oxidation of N_C-FeNi(OH)$_2$, N_I-FeNi(OH)$_2$, N_C-FeNi(OH)$_2$-1 and N_C-FeNi(OH)$_2$-2 and (b) LSV profiles for the freshwater OER and hydrazine oxidation of N_C-FeNi(OH)$_2$, N_I-FeNi(OH)$_2$, N_C-FeNi(OH)$_2$-1 and N_C-FeNi(OH)$_2$-2.

Table S2. Comparison of the OER activities of N_C-FeNi(OH)$_2$ with literature reported catalysts.

| Catalyst	Seawater overpotential	Freshwater overpotential	Current density (mA cm^{-2})	Reference
N_C-FeNi(OH)$_2$	110 mV	90 mV	50	This work
Ni$_2$P-Fe$_2$P	305 mV	261 mV	100	Adv. Funct. Mater., 2021, **31**, 2006484.
NiIr-LDH	286 mV	279 mV	100	J. Am. Chem. Soc., 2022, **144**, 9254-9263.
S-NiFe(O)OH	300 mV	281 mV	100	Energy Environ. Sci., 2020, **13**, 3439-3446.
FeOOH$_{0.60}$/Ni(HCO$_3$)$_2$	251 mV	216 mV	100	Nano Research, 2023, **16**, 2094-2101.
Fe$_2$P/Ni$_3$N	225 mV	219 mV	100	Small 2023, 19, 2207082.
NiFeS	226 mV	215 mV	100	J. Mater. Chem. A, 2023, **11**, 1116-1122.
NiMoN@NiFeN	307 mV	277 mV	100	Nat. Commun., 2019, **10**, 5106.
MnCo/NiSe	261.3 mV	225.8 mV	10	Appl. Catal. B: Environ., 2023, **325**, 122355.
CoFe$_2$O$_4$	286.2 mV	273.9 mV	100	Inorg. Chem., 2021, **60**, 17371–17378.
MoN–Co$_2$N	357 mV	267 mV	100	ACS Appl. Mater. Interfaces, 2022, **14**, 41924–41933.
Cu-NiCoP	250 mV	230 mV	10	J. Alloys and Compd., 2023, **966**, 171516.
FeP	287.1 mV	207 mV	10	Fuel, 2024, **369**, 131725.
NiTe@FeOOH	280 mV	264 mV	100	Chem. Eng. J., 2023, **474**, 145568.
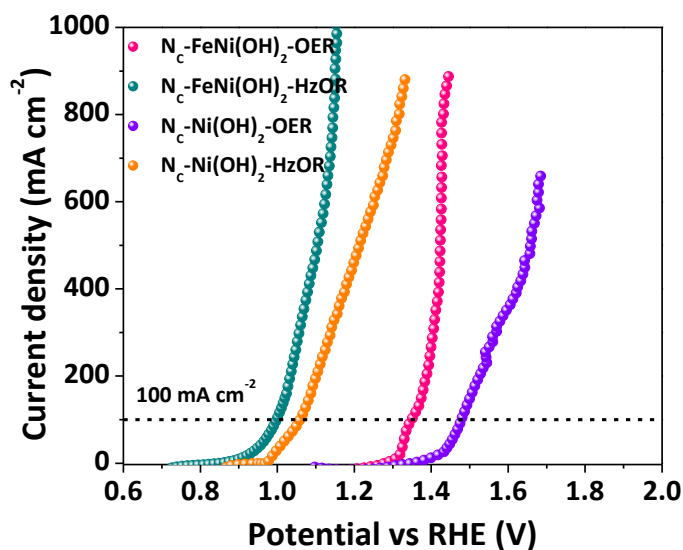
Figure S17. LSV profiles of N_C-FeNi(OH)$_2$ and N_C-Ni(OH)$_2$ showing the oxygen evolution and hydrazine oxidation activity in freshwater in the presence and absence of hydrazine.
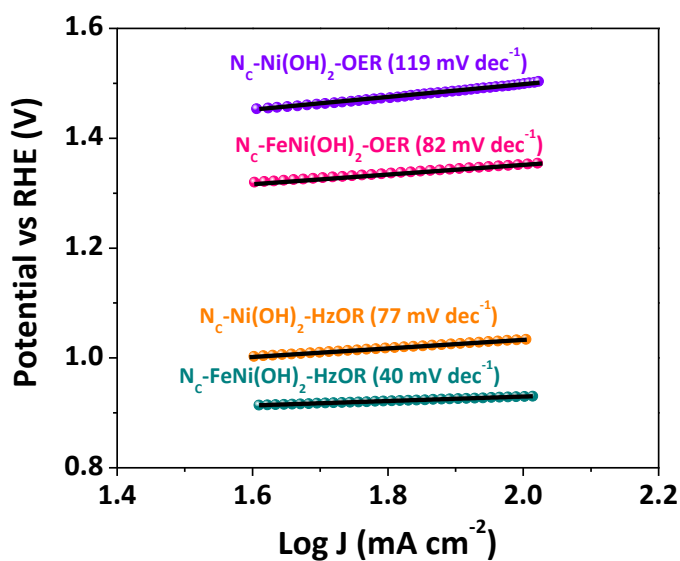

Figure S18. Tafel plots of N_C-FeNi(OH)$_2$ and N_C-Ni(OH)$_2$ for the oxygen evolution and hydrazine oxidation in real seawater in the presence and absence of hydrazine.

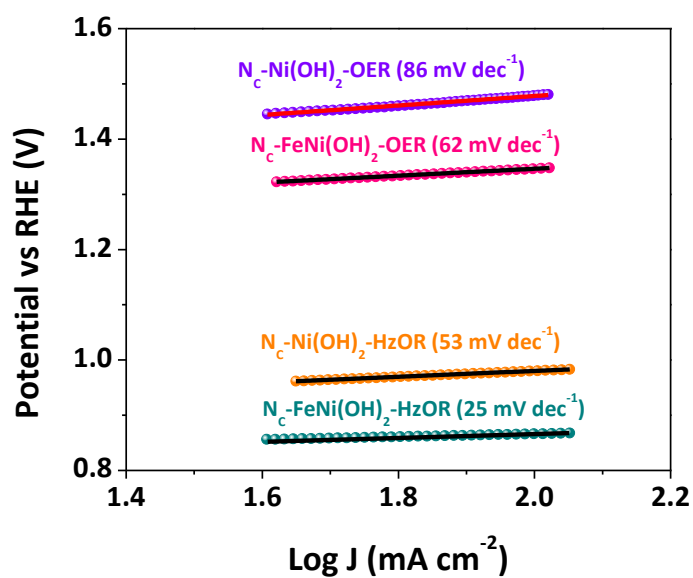**Figure S19.** Tafel plots of N_C-FeNi(OH)$_2$ and N_C-Ni(OH)$_2$ for the oxygen evolution and hydrazine oxidation in freshwater in the presence and absence of hydrazine.
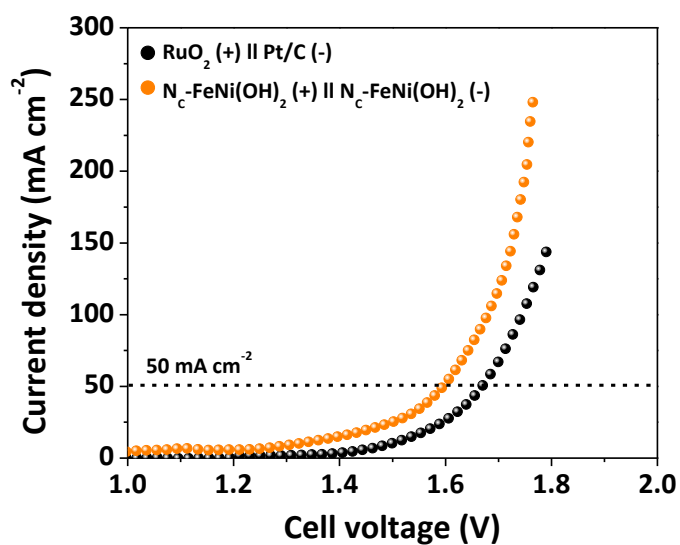

Figure S20. LSV profiles for the overall water splitting activity of N_C-FeNi(OH)$_2$ (orange) and Pt/C-RuO$_2$ (black) in real seawater.
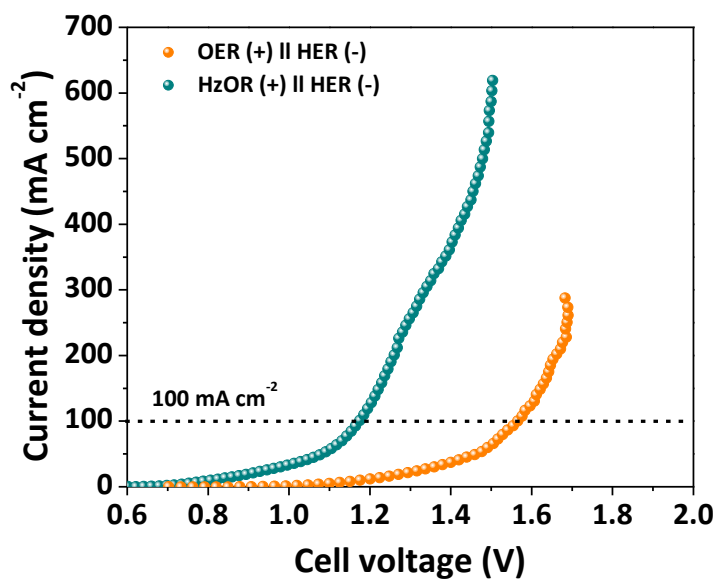
Figure S21. LSV profiles for the overall water splitting in the presence (cyan) and absence (orange) of hydrazine in two-electrode system in fresh water using N_C-FeNi(OH)$_2$ at the cathode and anode.
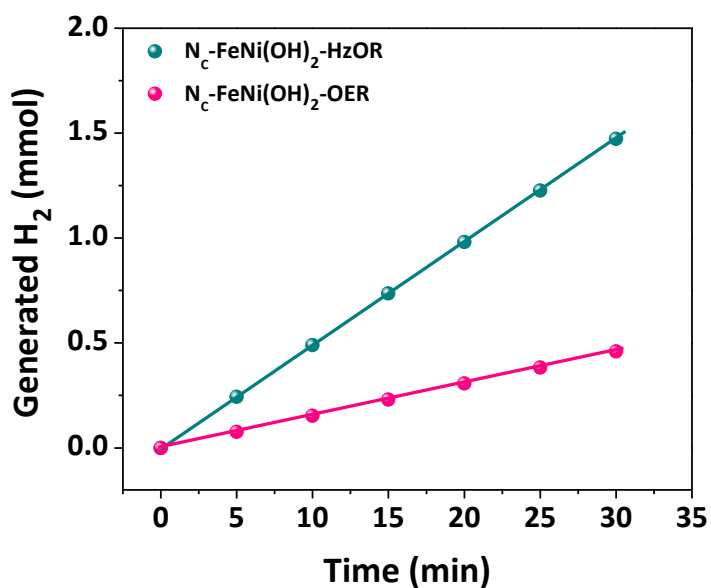

Figure S22. Amount of hydrogen produced during OER (magenta) and hydrazine oxidation (cyan) using N_C-FeNi(OH)$_2$ at the cathode and anode in two-electrode system.

Determination of Faradaic Efficiency in Fresh Water

The oxygen produced at the anode during the oxygen evolution reaction (OER) was measured using the water displacement method in an H-type cell. This was done over a period of 1800 seconds with a current density of 50 mA cm^{-2}. First, the theoretical amount of oxygen (O_2) was calculated based on Faraday's law using the following formula:

$$nO_2 = \frac{Q}{n \times F} = \frac{I \times t}{n \times F} = \frac{0.05 \times 1800}{4 \times 96485.3 \text{ s A mol}^{-1}} = 0.233 \text{ mmol}$$

During the chronoamperometric measurements, the actual amount of O_2 produced was recorded. This experimentally measured amount of O_2 was then compared to the theoretically calculated amount. The Faradaic efficiency was calculated using the following equation:

$$\text{Faradaic efficiency (\%)} = \frac{nO_2 \text{ (experimental)}}{nO_2 \text{ (theoretical)}} \times 100 = \frac{0.230 \text{ mmol}}{0.233 \text{ mmol}} \times 100 = 98.7\%$$
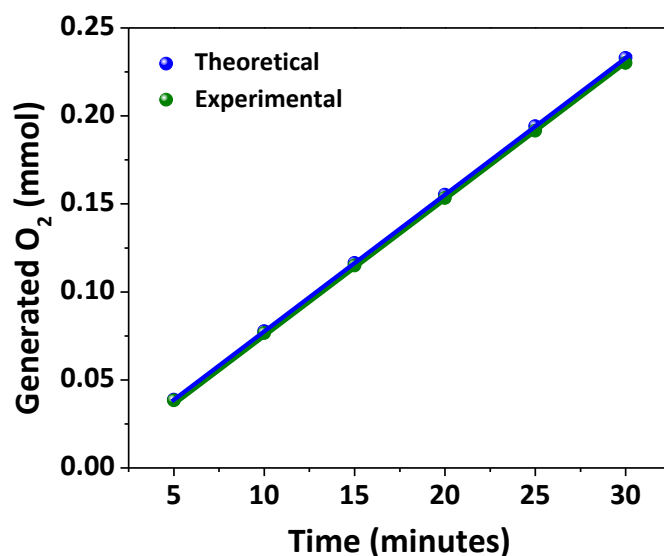

Figure S23. Amount of oxygen produced during OER theoretically and experimentally.

Determination of Faradaic Efficiency in Seawater

The oxygen produced at the anode during the oxygen evolution reaction (OER) was measured using the water displacement method in an H-type cell. This was done over a period of 1800 seconds with a current density of 50 mA cm^{-2}. First, the theoretical amount of oxygen (O_2) was calculated based on Faraday's law using the following formula:

$$nO_2 = \frac{Q}{n \times F} = \frac{I \times t}{n \times F} = \frac{0.05 \times 1800}{4 \times 96485.3 \text{ s A mol}^{-1}} = 0.233 \text{ mmol}$$

During the chronoamperometric measurements, the actual amount of O_2 produced was recorded. This experimentally measured amount of O_2 was then compared to the theoretically calculated amount. The Faradaic efficiency was calculated using the following equation:

$$\text{Faradaic efficiency (\%)} = \frac{nO_2 \text{ (experimental)}}{nO_2 \text{ (theoretical)}} \times 100 = \frac{0.229 \text{ mmol}}{0.233 \text{ mmol}} \times 100 = 98.2\%$$
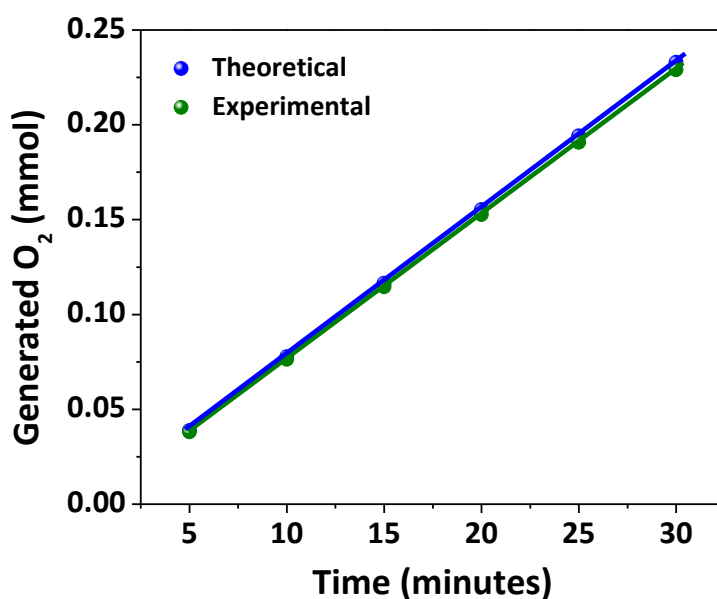

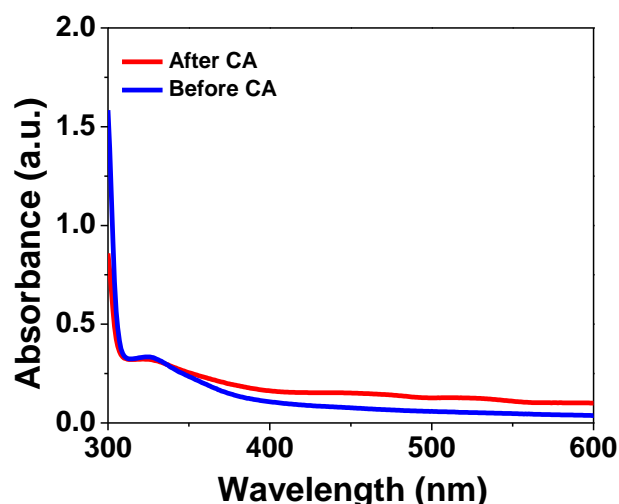**Figure S24.** Amount of oxygen produced during OER theoretically and experimentally.

Figure S25. The UV-Vis spectra of o-tolidine in seawater before and after electrochemical seawater splitting. The o-tolidine test was used to detect ClO^- in the electrolyte solution. When o-tolidine solution was added to the seawater electrolyte collected after the CA, there was no color change, indicating that ClO^- was not present. Additionally, the UV-Vis analysis of this mixture showed no absorption band at 437 nm.
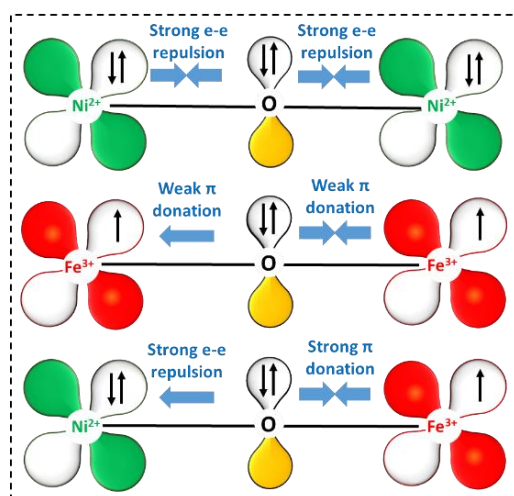

Figure S26. Schematic illustration showing the electronic interplay between the Ni^{2+} and Fe^{3+} sites.[2,5,7] The Ni^{2+} in a low spin state with $t_{2g}^6 e_g^2$ configuration possessed paired electrons, making the strong e−e repulsion with bridging O^{2-} ligand. Further, Fe^{3+} site with high spin state $t_{2g}^3 e_g^2$ resulted in the weak π-donation through O^{2-} bridging ligand. After the coupling between high spin Fe^{3+} and low spin Ni^{2+}, the strong π-donation was observed towards Fe^{3+} enhanced by the strong e−e repulsion of Ni^{2+}−O^{2-} bridge, promoting the partial electron transfer between the Ni and Fe sites.
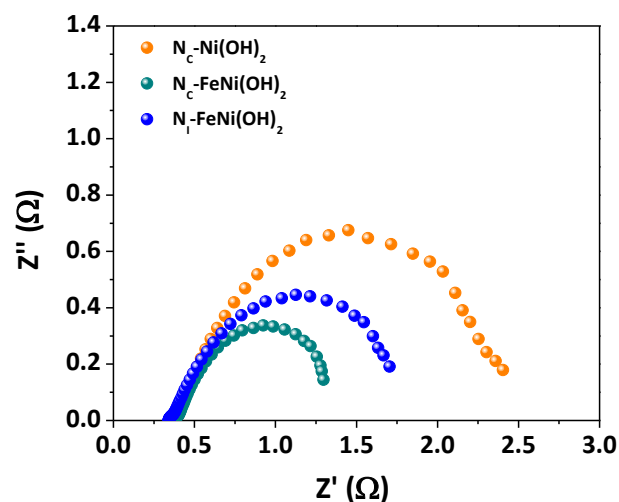
Figure S27. EIS plot of N_C-FeNi(OH)$_2$ (orange), N_I-FeNi(OH)$_2$ (blue), and N_C-Ni(OH)$_2$ (cyan) in real seawater.

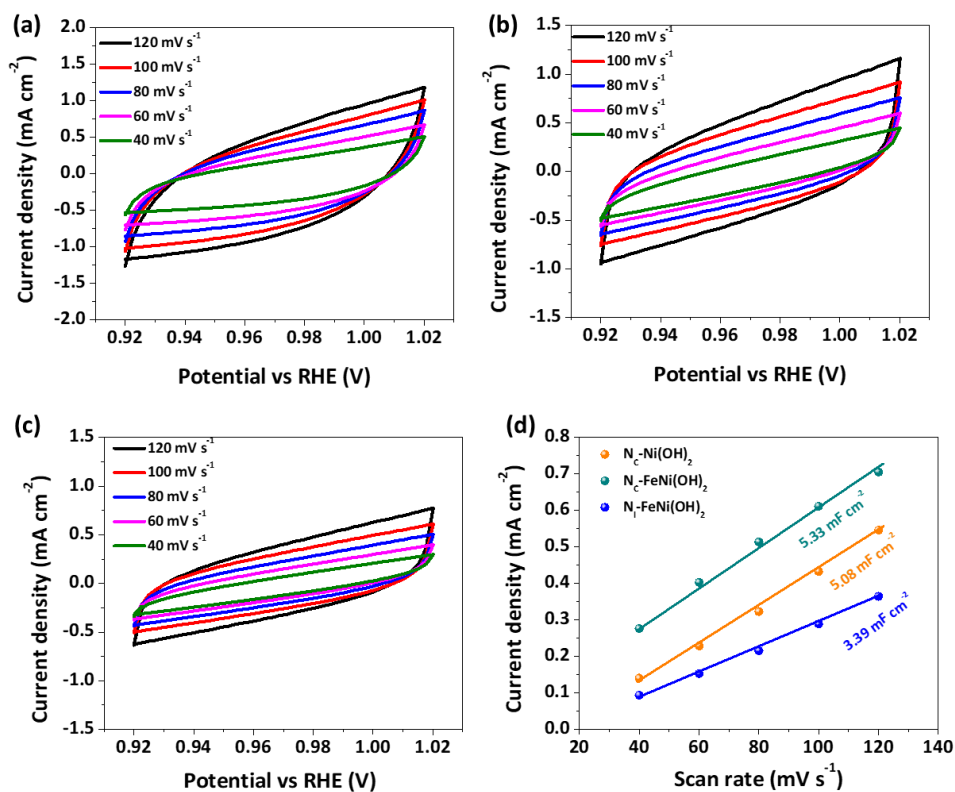**Figure S28.** Electrochemical capacitance current of (a) N_C-FeNi(OH)$_2$,(b) N_C-Ni(OH)$_2$ and (c) N_I-FeNi(OH)$_2$ in the non-Faradaic potential range of 0.92 V to 1.02 V vs RHE and (d) determination of double-layer capacitance (C_{dl}) by plotting (difference in current density)/2 against scan rate.
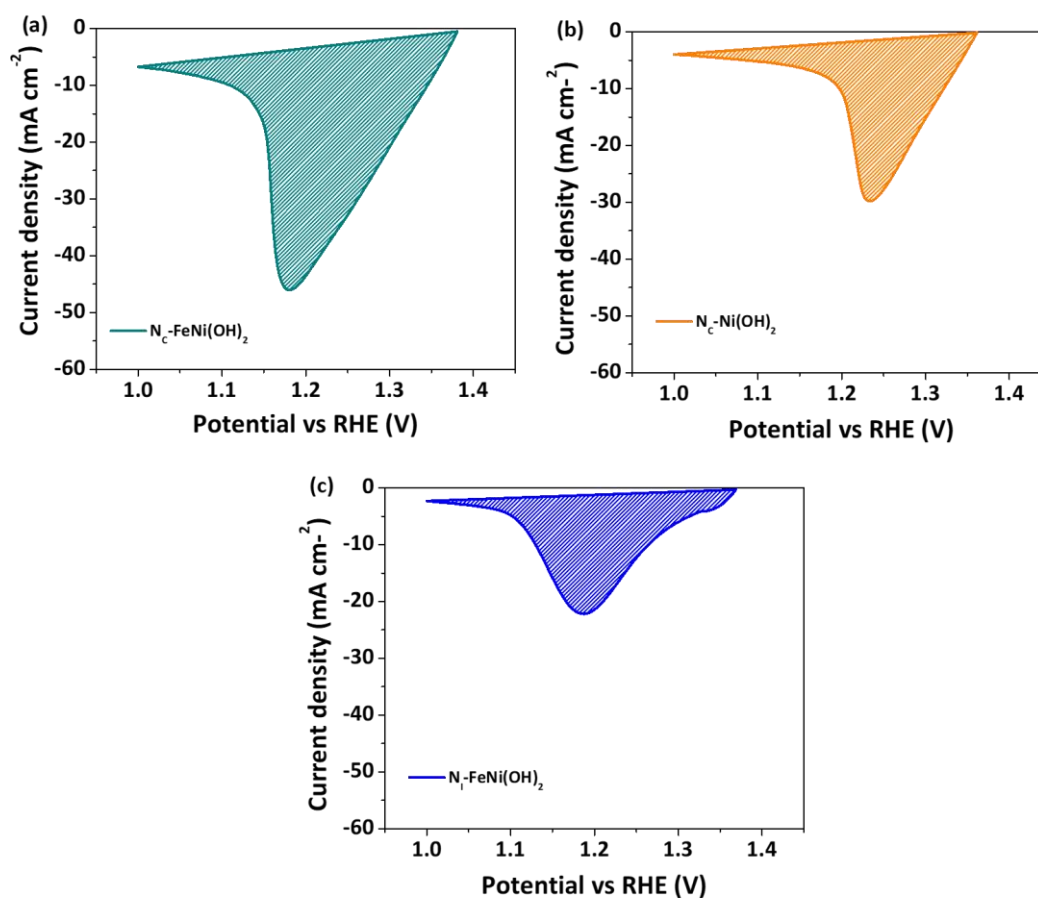
Figure S29. Reduction peak area utilized for the determination of number of active Ni sites in (a) N_C-FeNi(OH)$_2$,(b) N_C-Ni(OH)$_2$, and (c) N_I-FeNi(OH)$_2$.[8,9]

Equation S1. Determination of surface-active sites

For N_C-FeNi(OH)$_2$

Calculated area associated with the reduction peak = 6.0487 × 10^{-3} V A

Hence the associated charge is = 6.0487 × 10^{-3} V A / 0.005 V s^{-1}

$$= 1209.74 \times 10^{-3} \text{ A s}$$

$$= 1209.74 \times 10^{-3} \text{ C}$$

Now, the number of electron transferred is = 1209.74 × 10^{-3} C / 1.602 × 10^{-19} C

$$= 7.55 \times 10^{18}$$

Since the reduction of Ni^{3+} to Ni^{2+} is a single electron transfer reaction, the number of electrons calculated above is the same as the number of surface-active sites.

Hence, the surface-active Ni^{3+} sites is = **7.55 × 10^{18}**

For N$_C$-Ni(OH)$_2$

Calculated area associated with the reduction peak = 3.1387 × 10^{-3} V A

Hence the associated charge is = 3.1387 × 10^{-3} V A / 0.005 V s^{-1}

$$= 627.74 × 10^{-3} \text{ A s}$$

$$= 627.74 × 10^{-3} \text{ C}$$

Now, the number of electron transferred is = 627.74 × 10^{-3} C / 1.602 × 10^{-19} C

$$= 3.91 × 10^{18}$$

The surface-active Ni^{3+} sites participated is = **3.91 × 10^{18}**

For N$_I$-FeNi(OH)$_2$

Calculated area associated with the reduction peak = 2.8401 × 10^{-3} V A

Hence the associated charge is = 2.8401 × 10^{-3} V A / 0.005 V s^{-1}

$$= 568.02 × 10^{-3} \text{ A s}$$

$$= 568.02 × 10^{-3} \text{ C}$$

Now, the number of electron transferred is = 568.02 × 10^{-3} C / 1.602 × 10^{-19} C

$$= 3.54 × 10^{18}$$

Since the reduction of Ni^{3+} to Ni^{2+} is a single electron transfer reaction, the number of electrons calculated above is the same as the number of surface-active sites.

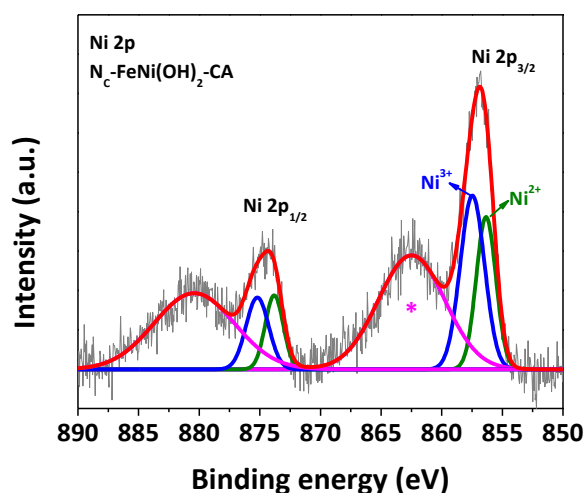Hence, the surface-active Ni^{3+} sites is = **3.54 × 10^{18}**

Figure S30. Ni 2p XPS of N_C-FeNi(OH)$_2$ after CA-stability test. The peaks at 856.92 eV and 874.29 eV in N_C-FeNi(OH)$_2$ correspond to Ni 2p$_{3/2}$ and Ni 2p$_{1/2}$, respectively.[2,5] The Ni^{2+} and Ni^{3+} peaks were observed at 856.34 eV and 857.49 eV. The Ni 2p$_{3/2}$ XPS peak in N_C-FeNi(OH)$_2$ showed a shift of 0.54 eV towards higher binding energy compared to the fresh N_C-FeNi(OH)$_2$. In addition, the peak intensity of Ni^{3+} was also increased suggesting the presence of large amount of Ni^{3+} after catalysis. * marked peak was ascribed to the satellite peak.[2,5]
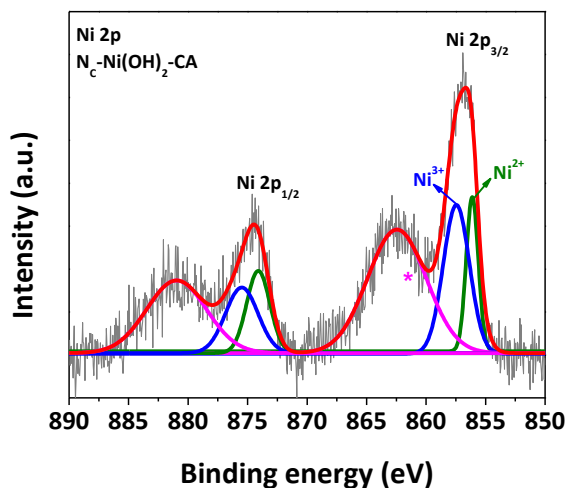

Figure S31. Ni 2p XPS of N_C-Ni(OH)$_2$ after CA-stability test. The peaks at 856.69 eV and 874.44 eV in N_C-Ni(OH)$_2$ correspond to Ni 2p$_{3/2}$ and Ni 2p$_{1/2}$, respectively.[2,5] The Ni^{2+} and Ni^{3+} peaks were observed at 856.12 eV and 857.42 eV. The Ni 2p$_{3/2}$ XPS peak in N_C-Ni(OH)$_2$ showed a shift of 0.77 eV towards higher binding energy compared to the fresh N_C-Ni(OH)$_2$. In addition, the peak intensity of Ni^{3+} was also increased suggesting the presence of large amount of Ni^{3+} after catalysis. * marked peak was ascribed to the satellite peak.[2,5]

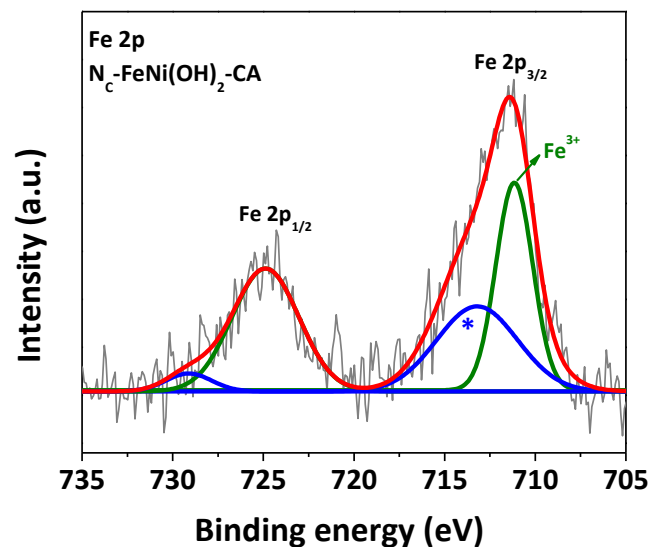**Figure S32.** Fe 2p XPS of N_C-FeNi(OH)$_2$ after CA-stability test. The peaks at 711.49 eV and 724.90 eV originated for Fe 2p$_{3/2}$ and Fe 2p$_{1/2}$, respectively. The peak at 711.43 eV was attributed to the Fe^{3+} species. The Fe 2p$_{3/2}$ peak was observed to be shifted by 0.38 eV compared to the fresh catalyst indicating the presence of more amount of high valent Fe ions after catalysis.[3,4]
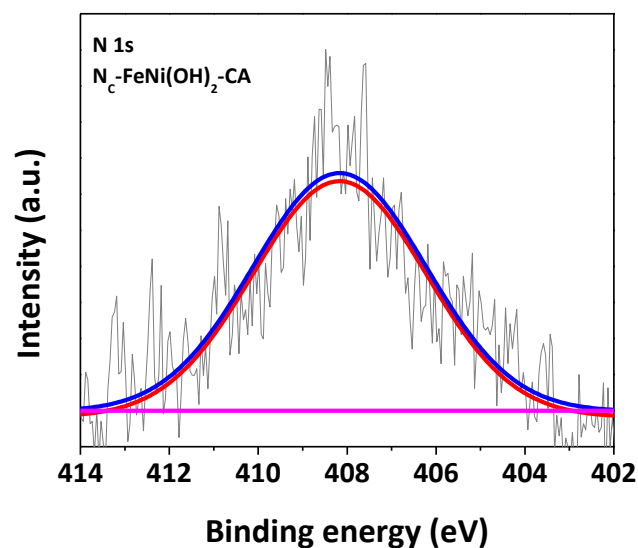

Figure S33. N 1s XPS of N_C-FeNi(OH)$_2$ after CA-stability test showing the peak at 408.15 eV corresponding to the metal-nitrate bond.[2]
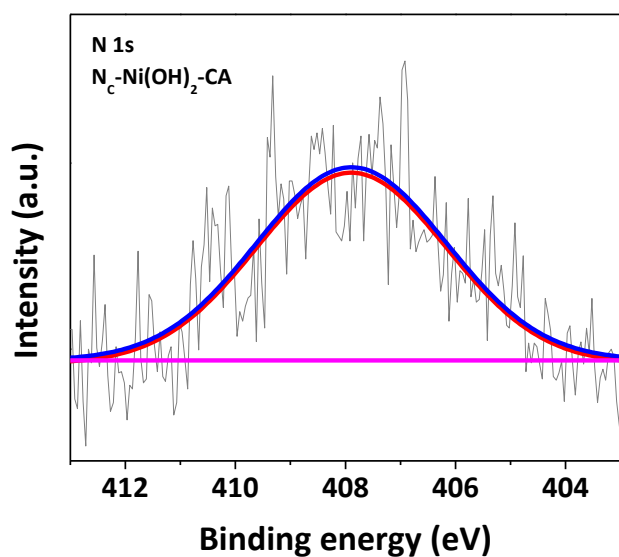
Figure S34. N 1s XPS of N_C-Ni(OH)$_2$ after CA-stability test showing the peak at 407.90 eV corresponding to the metal-nitrate bond.[2]
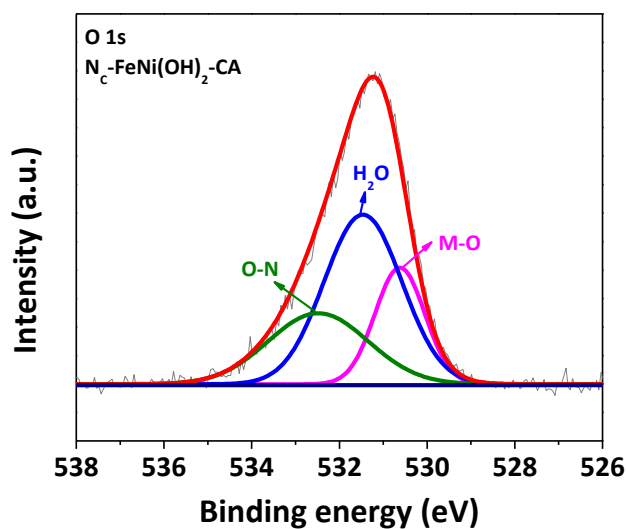

Figure S35. O 1s XPS of N_C-FeNi(OH)$_2$ after CA-stability test. The peaks were originated for M-OH group (530.16 eV), absorbed water on the surface (531.46 eV) and O–N bond from NO$_3^-$ (532.48 eV). The O 1s XPS was shifted by 1.53 eV towards lower binding energy compared to the fresh catalyst.[3,4]
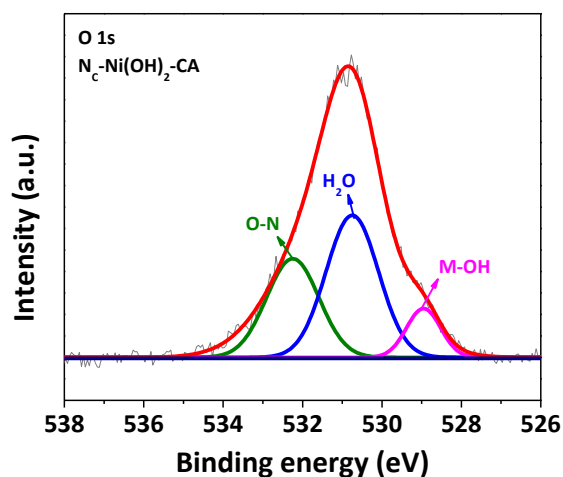
Figure S36. O 1s XPS of N_C-Ni(OH)$_2$ after CA-stability test. The peaks were originated for M-OH group (528.94 eV), adsorbed water on the surface (530.72 eV) and O–N bond from NO$_3^-$ (532.24 eV). The O 1s XPS was shifted by 0.31 eV towards lower binding energy compared to the fresh catalyst.[3,4]
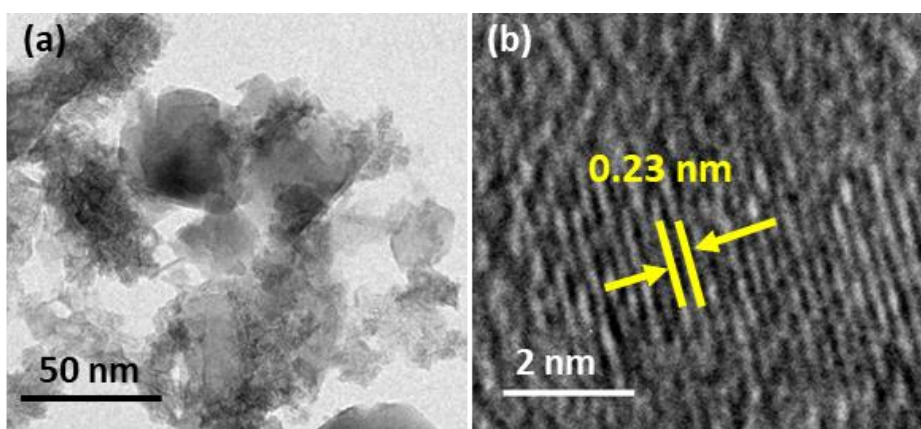

Figure S37. (a) TEM image of N_C-FeNi(OH)$_2$ after CA-stability test showing the agglomerated nanosheet morphology and (b) HRTEM image of N_C-FeNi(OH)$_2$ after CA-stability showing the 0.23 nm d-spacing.

References

1   S. Dutta, A. Indra, Y. Feng, T. Song and U. Paik, *ACS Appl. Mater. Interfaces*, 2017, **9**, 33766–33774.

2   Y.-N. Zhou, F.-T. Li, B. Dong and Y.-M. Chai, *Energy Environ. Sci.*, 2024, **17**, 1468–1481.

3   B. Singh, O. Prakash, P. Maiti, P. W. Menezes and A. Indra, *Chem. Commun.*, 2020, **56**, 15036–15039.

4   B. Singh, P. Mannu, Y. C. Huang, R. Prakash, S. Shen, C. L. Dong and A. Indra, *Angew. Chem. Int. Ed.*, 2022, **62**, e202211585.

5   H. Sun, J. G. Li, L. Lv, Z. Li, X. Ao, C. Xu, X. Xue, G. Hong and C. Wang, *J. Power Sources*, 2019, **425**, 138–146.

6   Z. Chen, Q. Fan, M. Huang and H. Cölfen, *Small*, 2023, **19**, 2300509.

7   L. Zhuang, L. Ge, H. Liu, Z. Jiang, Y. Jia, Z. Li, D. Yang, R. K. Hocking, M. Li, L. Zhang, X. Wang, X. Yao and Z. Zhu, *Angew. Chem.*, 2019, **131**, 13699–13706.

8   S. Anantharaj and S. Kundu, *ACS Energy Lett.*, 2019, **4**, 1260–1264.

9   S. Anantharaj, S. R. Ede, K. Karthick, S. Sam Sankar, K. Sangeetha, P. E. Karthik and S. Kundu, *Energy Environ. Sci.*, 2018, **11**, 744–771.